Stability Assessment of A Droop-Controlled Multi-Generator Electrical Power System in the More Electric Aircraft Using Parameter Space Approach

Fei Gao[1], Xiancheng Zheng[2], and Serhiy Bozhko[1]
1.Power Electronics, Machines and Control Research Group, The University of Nottingham, Nottingham, UK.
2. School of Automation, Northwestern Polytechnical University, Xi'an, China.

***Abstract*— This paper investigates the dynamic stability of a droop-controlled multi-generator system in the more electric aircraft (MEA). Based on the developed state-space model of the potential dc electrical power system (EPS) architecture, the stability boundaries of EPS operation depending on parameter variations including component parameters and operating conditions are investigated. The effect of multiple parametric uncertainties on EPS stability is graphically illustrated by stability regions maps. In addition, the effect of the droop coefficient on the stability is discussed from the impedance point of view. The detailed mathematical models and analytical results of stability assessment are verified by time domain simulation studies.**

***Keywords*— Parameter space method, stability, droop control, constant power load, more electric aircraft, multi-generator system.**

I. INTRODUCTION

The concept of more-electric aircraft (MEA) which assumes use of electrical power to replace the conventional mechanical and hydraulic powers onboard the aircraft is widely accepted in recent years [1], [2]. The electrical power system (EPS) for the MEA is a hot topic for researchers in this targeting field. Among different distribution structures, DC distribution EPS structure is promising due to lower system cost, better efficiency and absence of reactive power compensation devices [3], [4]. Typical loads in such system are tightly controlled by power electronics and often behave like constant power loads (CPLs). Since CPLs have negative incremental impedance characteristic [5], stability of such EPS is a great challenge for the system designers [6]-[8]. Several publications have studied small signal stability of MEA EPS. In [9], stability for hybrid ac-dc MEA EPS is investigated and the influence of parameters variations on system stability is presented. However, droop control is not included since only single generator operation is taken into account in this study. Stability of a 270 V dc EPS has been analyzed in [10]. A switch reluctance motor is used in the considered system rather than a permanent magnet synchronous generator (PMSG). In modern EPS, multiple generators taking power from the main engine are used as the sources to supply the main bus(es) and loads. Appropriate power sharing among the sources is of great importance in the multi-generator system. Droop control, a typical decentralized control method, has been widely used due to its modularity, reliability and absence of communication links [11].

When dealing with the practical system, the expected perturbations needs to be taken into account since the uncertainties can always occur. The uncertain parameters are either physical quantities or control dynamics. Since usually more than one parameter will change, the parameter space approach was proposed due to the ease of visualization. So far, the parameter space method has been widely accepted for robust control design [12]-[14]. However, this task can be addressed by parameter space method which is easier to interpret due to its graphical nature and convenience of the results visualization. In this paper we apply this method for stability study of multi-generator MEA EPS under droop control. The aim is to solve the problem of determining system parameters variations that lead to unstable effects, as well as to design controller that keeps the system stable under such variations.

The main contribution of this paper can be highlighted as follows:

The research was supported by the CleanSky JTI Project, a FP7 European Integrated Project-http://www.cleansky.eu.

(1) State-space model development for a droop-controlled twin-generator system in the MEA.

(2) Parameter space mapping for uncertainties in component parameter, control parameter and operating parameter.

II. System Architecture and Modeling

Fig. 1 shows the generalized potential architecture of multi-generator dc EPS for MEA. As one can see, the twin generators (PMSGs-G_1 and G_2) take power from the main engine via high pressure (HP) and low pressure (LP) shaft, and operate in parallel to transfer the electrical power to the main dc bus. Both generators are vector-controlled and are operated at high-speed region in flux-weakening mode [15]. The common 270 V dc bus is powered by dual generation channels G_1 and G_2, which are controlled by pulse-width modulated (PWM) active rectifiers AR_1-AR_2 correspondingly. In Fig. 1 C_1-C_2 correspond to the local converter output capacitors (local buses) and C_b is a capacitor bank installed on the main bus bar. The cumulative load represents the power electronic interfaced loads which consist of CPLs and resistive loads. Droop characteristic is used in each generator-converter channel to ensure current sharing between sources and the feasible dc bus voltage specifications is described in [16].

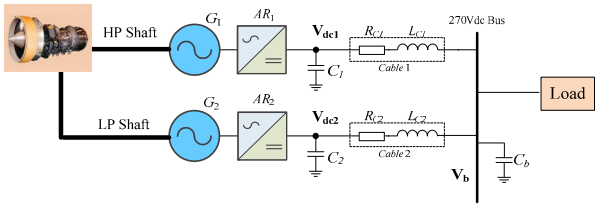

Fig. 1. Configuration of the system under study.

Fig. 2 illustrates the inner control loop of the system. As one can see, fundamental vector control is used in the core system. After transforming measured currents to rotating frame, conventional PI controller adjusts current in the *dq* domain and outputs *dq* voltage demands. Voltage demands are inversely transformed into 3-phase demand modulation indexes for PWM. Then the core system can be fully controlled by using both *dq* current demands. As can be seen from Fig. 3, for the outer loop control, conventional PI controllers are used to deflux the machine (*d*-axis) and control the output DC current (*q*-axis). The stator current references in *d* and *q* axes are obtained from the output of the flux weakening controller and I_{dc} controller respectively. The reference of the ac voltage (v_c) is dependent on the DC voltage. The DC current reference (i_{dc}^{ref}) is obtained by the desired droop characteristic.

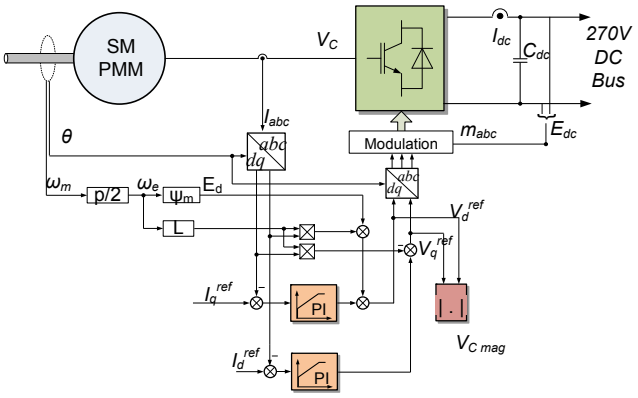

Fig. 2. Inner current loop for the PMSG-AR.

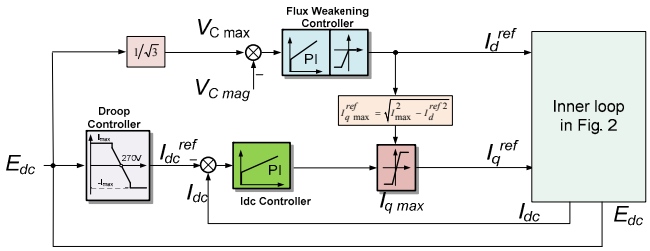

Fig. 3. Outer control loop for the PMSG-AR.

A. PMSG and Converter Model

The dynamic equations for PMG in synchronous *dq* frame aligned with the rotor position are given by [15]:

$$\begin{cases} L_d \dfrac{di_d}{dt} = v_d - R_s i_d + \omega_e L_q i_q \\ L_q \dfrac{di_q}{dt} = v_q - R_s i_q - \omega_e L_d i_d - \omega_e \phi_m \end{cases} \tag{1}$$

where v_d ,v_q are the respective *d*-axis, *q*-axis component of stator voltage; i_d ,i_q are the respective *d*-axis, *q*-axis component of stator current; R_s is the stator resistance; ϕ_m is the flux linkage of permanent magnet; ω_e is the electrical rotor angular velocity.

According to the control block diagram in Fig. 2, one can get the equation (2) with X_{vci} , X_{ioi}, X_{idi}, X_{iqi} as the state variables for PI controller parameters of flux weakening controller, current sharing controller and *d*-axis and *q*-axis current controllers, respectively.

$$\begin{cases} \dot{X}_{vci} = v^*_{cmax} - v_c \\ \dot{X}_{ioi} = i^{ref}_{dc} - i_o \\ \dot{X}_{idi} = K_{vci}X_{vci} + K_{vcp}v^*_{cmax} - K_{vcp}v_c - i_d \\ \dot{X}_{iqi} = K_{ioi}X_{ioi} + K_{iop}i^{ref}_{dc} - K_{iop}i_o - i_q \end{cases} \quad (2)$$

where v_c is the ac side voltage of the converter.

B. DC-Link Model

Based on the control scheme shown in Fig. 2, the dc current reference for each source is generated by the droop characteristic, as shown in Fig. 4. The linear area of this characteristic is of interest where its slope is can be represented by the gain k_{Di}. The current reference ($I_{dci}{}^{ref}$) can be written as

$$I^{ref}_{dci} = (V_o - V_b)k_{Di} \quad i = 1,2 \quad (3)$$

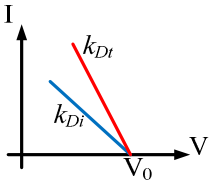

Fig. 4. Droop characteristic.

The converter dynamic (G_{Dyi}), which is the current tracking performance, can be expressed as follows:

$$G_{Dyi} = \frac{I_{dci}}{I^{ref}_{dci}} \quad (4)$$

The equation of the current control dynamics is already derived in [17]. The equivalent circuit for two sources operating in parallel can be illustrated by equivalent circuit in Fig. 5. R_{c1}-L_{c1} and R_{c2}-L_{c2} represent the cable resistance and inductance from AR_1, AR_2 to the main bus, respectively.

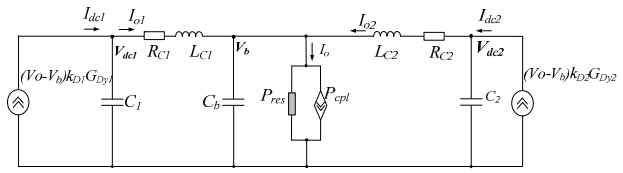

Fig. 5. Equivalent circuit for parallel sources.

The ordinary differential equations of the circuit can be expressed as follows:

$$\begin{cases} L_{c1}\dfrac{di_{o1}}{dt} = v_{dc1} - R_{c1}i_{o1} - v_b \\ L_{c2}\dfrac{di_{o2}}{dt} = v_{dc2} - R_{c2}i_{o2} - v_b \\ C_b\dfrac{dv_b}{dt} = i_{o1} + i_{o2} - i_o \end{cases} \quad (5)$$

C. Load Model

In this paper the EPS load is a combination of ideal resistive P_{res} and ideal CPL P_{CPL}. The total load power therefore can be represented as follows:

$$P_L = P_{res} + P_{cpl} = \frac{V_b^2}{R_{res}} + P_{cpl} \quad (6)$$

The total load current yields:

$$i_o = \frac{v_b}{R_{res}} + \frac{P_{cpl}}{v_b} \quad (7)$$

The small signal load current can be expressed as follows:

$$\hat{i}_o = \left(\frac{2}{R_{res}} - \frac{P_{cpl}}{V_b^2}\right)\hat{v}_b \quad (8)$$

III. MAPPING PROCEDURE

Parameter space method is an analytical technique to perform system analysis for a control system [13]. Using this method, a direct correlation between roots of the characteristic equation and the uncertain parameters is determined in a manner suitable for a graphical display in the parameter space. The flowchart of mapping procedure the steps are discussed as follows.

Step 1) Equilibrium point calculation

For a complex non-linear system, the equilibrium point calculation can be obtained by solving the set of the equations from the system modelling. In addition, the limitation due to the practical operation scenario and ratings of the equipment

should be taken into account to get the feasible operating point.

Step 2) Linearized model derivation

For a non-linear system, the linearized state-space model in small signal can be developed according to the specific equilibrium point.

Step 3) Eigenvalues calculation of the state-space matrices

The eigenvalues of the small signal model obtained by linearizing the system around an equilibrium point can be calculated to evaluate the local stability. If the real parts of all the matrix eigenvalues are negative, the corresponding equilibrium point is stable. Otherwise, the system is not locally stable.

Step 4) Mapping the point into corresponding parameter plane

In the general case of two uncertain parameters, the stability region can be mapped into a plane of the two parameters. After the abovementioned three steps, the stability regions are mapped into a plane of two parameters which can be associated with uncertain physical parameters, control parameters or operating point. The mapping algorithm will determine the local stability of a set of equilibrium points. Those equilibrium points will be classified into two categories: stable equilibrium points, or unstable equilibrium point. The feasible region is the set of equilibrium points that can be reached from a stable equilibrium point by means of a smooth parameter variation.

A. Equilibrium Point Calculation

Following the abovementioned procedure, operating point calculation is the first step to confirm the local stability condition. For the system shown in Fig. 1, the equilibrium point calculation can be divided into dc side and ac side.

1) DC operating point

As it can be seen from Fig. 4, the relationship of total load current can be expressed as:

$$I_o - P_{cpl} / V_b - P_{res} / V_b = 0 \tag{9}$$

where V_b and I_o are the bus voltage and load current respectively.

In steady state, the dc current reference is obtained by the droop characteristic which can be expressed as follows:

$$I_{dci}^{ref} = I_{oi} = (V_o - V_b)k_{Di} \quad i = 1,2, \quad I_o = I_{o1} + I_{o2} \tag{10}$$

where I_{oi} is the output current for each generation channel and I_o is the total load current.

The local voltage can be derived as follows using Fig. 5:

$$V_{dci} = V_b + I_{oi} R_{ci} \tag{11}$$

where V_{dci} is the voltage of the local capacitor C_i.

Based on the standard MIL-STD-704F [16], the dc bus voltage in steady-state should satisfy the range between 250V and 280V. Thus, the constraint condition for the dc side yields:

$$250V \le V_b \le 280V \tag{12}$$

2) AC operating point

In steady state, the electromagnetic equations for the PMSGs are shown in (13),

$$\begin{cases} V_d + R_s I_d - \omega_e L_q I_q = 0 \\ V_q + R_s I_d + \omega_e L_d I_d + \omega_e \phi_m = 0 \end{cases} \tag{13}$$

where I_d, I_q are the d-axis, q-axis component of stator current; V_d, V_q are the d-axis, q-axis stator voltage and they satisfy the following relationship:

$$\sqrt{V_d^2 + V_q^2} \le V_{dc} / \sqrt{3} \tag{14}$$

The dc current with respect to modulation index yields:

$$I_{dc} = \frac{3}{4}(D_d I_d + D_q I_q) \tag{15}$$

where D_d, D_q are the modulation index satisfying the following relationship:

$$D_d = V_d / (0.5V_{dc}), D_q = V_q / (0.5V_{dc}) \tag{16}$$

Similarly, there are some constraints in ac side as well. The converter current has some limitations which can be expressed as

$$\sqrt{I_d^2 + I_q^2} \le 400A \tag{17}$$

The equilibrium point can be calculated by solving the equations (9)-(17). Since nonlinear set of equations may have more than one set of solutions, only one group of solution is feasible for the targeting power system. Hence, the constraint conditions (equations (12), (14), (17)) can be used to compute the practical equilibrium point.

B. Linearized Matrix in State-Space

The state-space model of the multi-generator EPS represented by Fig. 1 can be formulated as

$$\dot{\hat{\mathbf{X}}}_\mathbf{p} = \mathbf{A}_\mathbf{p}\hat{\mathbf{X}}_\mathbf{p} \tag{18}$$

where the states variables are shown as follows:

$$\begin{aligned}\hat{\mathbf{X}}_\mathbf{p} = <\, &\hat{v}_{dc1}, \hat{i}_{d1}, \hat{i}_{q1}, \hat{X}_{vci1}, \hat{X}_{ioi1}, \hat{X}_{idi1}, \hat{X}_{iqi1}, \hat{i}_{o1}, \\ &\hat{v}_{dc2}, \hat{i}_{d2}, \hat{i}_{q2}, \hat{X}_{vci2}, \hat{X}_{ioi2}, \hat{X}_{idi2}, \hat{X}_{iqi2}, \hat{i}_{o2}, \hat{v}_b >\end{aligned} \tag{19}$$

The state matrix A_p will be of dimension 17*17 and can be given as in (22),

$$\mathrm{A_P} = \begin{bmatrix} A_1 & 0_{7*7} & E_1 & 0_{7*1} & F_1 \\ 0_{7*7} & A_2 & 0_{7*1} & E_2 & F_2 \\ L_1 & L_2 & L_3 & L_4 & L_5 \end{bmatrix} \tag{20}$$

where A_1 and A_2 of dimension 7*7 are the system matrices for two generation system; E_1 and E_2 of dimension 7*1 are the corresponding input matrices; L_1, L_2, L_3, L_4, and L_5 are the matrices related to the cables and loads. Details of the matrix elements are shown in Appendix A.

C. Eigenvalues Computation

It is known that the eigenvalues of the state matrix of the linearized system defines the stability of the equilibrium point. Based on the matrix $\mathbf{A_p}$. eigenvalues can be computed accordingly.

D. Parameter Space Mapping

The chosen parameter for visualization in the parameter plane can be operating condition (machine speed, load power) or plant parameters (e.g., cable impedances, bus capacitances and etc.). The nominal plant and control parameters are presented in Appendix B. The stability region for different parameters variations will be presented in next section.

IV. STABILITY EVALUATION FOR PARAMETER VARIATIONS

As previously mentioned, uncertain parameters in the entire system can be operating parameters (e.g. load power, machine speed), component parameters (cable impedance, bus capacitance etc.) and control parameters (droop coefficient). This section will discuss the effect of parameter variations in the three categories respectively.

A linearized CPL can be approximately expressed by a negative incremental impedance ($-R_{CPL}$) in parallel with a current source (I_{CPL}).

$$R_{CPL} = \frac{V_b^2}{P_{CPL}}, \quad I_{CPL} = 2\frac{P_{CPL}}{V_b} \tag{21}$$

where P_{CPL} is the power for the CPL.

A. Effect of Operating Parameter Variation

In the example EPS shown in Fig. 1, load is the combination of resistive load and CPL. Using the parameters in Appendix B, the stability region with respect to (w.r.t.) CPL and resistive load is presented in Fig. 6(a). It can be clearly seen that more resistive load is beneficial to keep system stable when CPL is over 60 kW assuming that the . It matches the fact that CPL will easily give rise to instability due to its negative incremental resistance characteristic. Furthermore, the machine speed can be considered as the operating parameter. The parameter space map w.r.t. CPL and generator speed is shown in Fig. 6(b). As one can see, the system with generator running above 22 krpm is unstable when the CPL exceeds 80 kW. As a short summary here, high speed and high CPL operation scenario has the least stability margin.

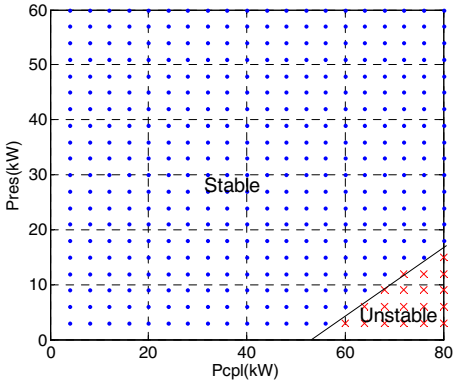

(a)

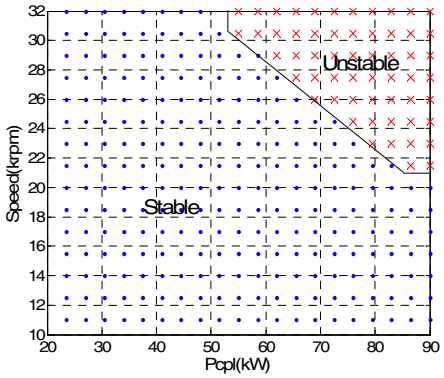

(b)

Fig. 6. Parameter space map for load characteristic. (a) CPL and resistive load. (b) CPL and generator speed.

B. *Effect of Component Parameter Variation*

Feeder impedance may also influence the system stability. Fig. 10 shows the effect of cable impedance on stability using parameter maps. Since more resistive cable increases the passive damping of the original system, system is more stable if the distribution cable is mainly resistive. It can be seen from Fig. 10 that the system is stable only if the ratio of cable resistance and inductance is over 3000. For example, if the feeder inductance is 2 μH, the system is stable when feeder resistance is over 6 mΩ.

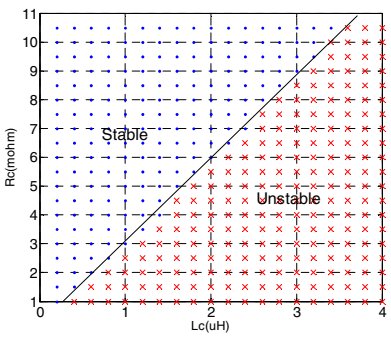

Fig. 7. Parameter space map w.r.t. cable resistance and inductance.

C. *Effect of Droop Coefficient*

The effect of droop coefficient variation on the source and load impedance is shown in Figs. 8 and 9. It is seen from Fig. 8 that the source impedance magnitude increases by increasing the droop coefficient, especially at low frequencies.

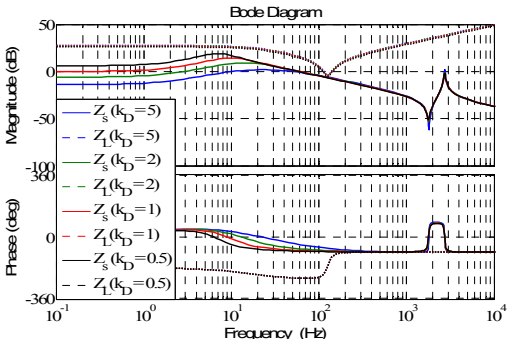

Fig. 8. Source impedance with different droop coefficients.

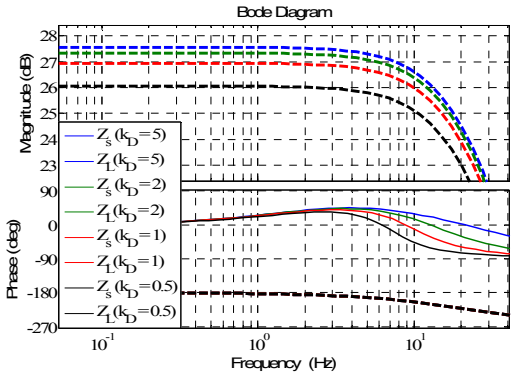

Fig. 9. Load impedance with different droop coefficients.

As can be inferred from (21), the load impedance magnitude at low frequency will be reduced due to the reduced bus voltage. It can be seen from Fig. 9 that the magnitude of the load impedance decreases with the decrease of the droop coefficient, which is in alignment with the analysis. Overall, it can be concluded that the system stability margin is reduced if a smaller droop coefficient is applied. The operating point of the dc bus voltage will be reduced further and as a result, the magnitude of the load impedance will decrease and consequently, reducing the stability margin.

As discussed in [17], the droop coefficient also has a higher boundary which is limited by a right half plane (RHP) zero:

$$z = -\frac{v_{qo} + R_s i_{qo} - \omega_e L_s i_{do}}{L_s i_{qo}} \tag{22}$$

where the subscript "o" represents the operating point of corresponding variables. Thus, due to the existence of this

RHP zero, a large droop coefficient would pose the challenge to system stability as well.

I. Results and Discussion

To validate the effectiveness of the proposed state-space model and parameter space method, this section shows the simulation results and stability condition of the twin-generator based system assuming that both generators have the same specifications and control parameters are identical.

A. *Effect of the Generator Speed*

Table I presents the simulation scenario. Fig. 10 shows the twin generator speed, total load current and dc bus voltage according to the scenario listed in Table I. Prior to t = 0.16 s, the system is working under 60 kW CPL with twin generators working at 15 krpm. The speed of twin generators increases from 20 krpm to 32 krpm between t = 0.16 s and 0.2 s. Onset of oscillation is visible after t = 0.18 s (25 krpm) and the system becomes unstable when both generators are operating at 32 krpm. It confirms that the high speed operation degrades the system stability. In addition, the impact of CPLs can be also observed from Fig. 10. As the CPL is reduced from 60 kW to 40 kW after t = 0.24 s, the damping of the system is reinforced and parallel system restores stable operation even in high speed region. The result validates the findings in Fig. 6 that the system at high speed, high power region is unstable.

TABLE I Simulation Scenario

Time (s)	Machine speed	CPL
Before 0.16 s	15 krpm	60 kW
0.16-0.18 s	20 krpm	60 kW
0.18-0.2 s	25 krpm	60 kW
0.2-0.24 s	32 krpm	60 kW
0.24-0.26 s	32 krpm	50 kW
0.26-0.28 s	32 krpm	40 kW

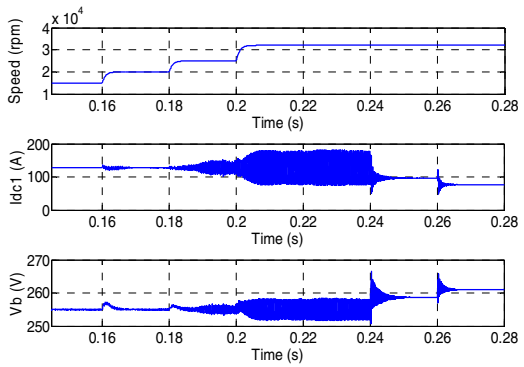

Fig. 10. Results of the system under machine speed and CPL variation.

B. *Effect of the Droop Coefficient*

In the following test, the droop coefficient (k_{Di}) is varied to investigate the effect of droop controller on stability. Fig. 11 presents the dc current and voltage for G_1. Before t = 0.04 s, the system is running at small droop coefficient (k_{Di} = 8.5). When a large droop coefficient is employed after t = 0.04 s, the dc voltage deviation is reduced, which is consistent with the droop characteristic (see (3)). The oscillation and eventual instability can be seen when large droop coefficients (k_{Di} = 70, 80) are employed between t = 0.06 s and t = 0.08 s. After t = 0.08 s, if the droop coefficient is modified to smaller values (k_{Di} = 10, 5), the parallel system can restore to stale operation again.

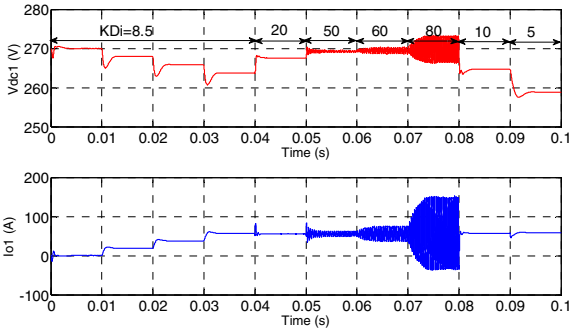

Fig. 11. Results of the system with droop coefficient variations.

II. Conclusion

In this paper, a parameter space method was applied for stability investigation of a twin-generator paralleled DC EPS in the future MEA. The procedure of the parameter space mapping is addressed and the state-space model of the droop-controlled multi-generator systems is developed. The main findings of this paper are as follows:

1) High generator speed and high CPL region jeopardizes the damping of the system and can be regarded to be the worst operating case for stability.

2) Due to the effect of RHP zero in the non-minimum phase system, a large droop coefficient will comprise the system stability. A small droop coefficient would increase the source impedance and reduce the load impedance and the consequently possible source/load impedance interaction may lead to instability as well. As a result, a proper range of the droop coefficient should be selected.

APPENDIX A

STATE MATRIX A_P OF THE TWIN GENERATOR SYSTEM

The matrix elements L_1-L_5 of (20) are shown below. The other submatrices A_1, A_2, E_1 and E_2 whose elements are consist of operating points, are too complex to show here.

$$L_1 = \begin{bmatrix} \frac{1}{L_{C1}} & 0 & 0 & 0 & 0 & 0 & 0 \\ 0 & 0 & 0 & 0 & 0 & 0 & 0 \\ 0 & 0 & 0 & 0 & 0 & 0 & 0 \end{bmatrix},$$

$$L_2 = \begin{bmatrix} 0 & 0 & 0 & 0 & 0 & 0 & 0 \\ \frac{1}{L_{C1}} & 0 & 0 & 0 & 0 & 0 & 0 \\ 0 & 0 & 0 & 0 & 0 & 0 & 0 \end{bmatrix}$$

$$L_3 = \begin{bmatrix} -\frac{R_{C1}}{L_{C1}} \\ 0 \\ \frac{1}{C_b} \end{bmatrix}, \quad L_4 = \begin{bmatrix} 0 \\ -\frac{R_{C2}}{L_{C2}} \\ \frac{1}{C_b} \end{bmatrix}, \quad L_5 = \begin{bmatrix} -\frac{1}{L_{C1}} \\ -\frac{1}{L_{C2}} \\ -\frac{(2V_b - R_L I_o)}{C_b R_L V_b} \end{bmatrix}$$

APPENDIX B

THE EPS PARAMETERS

Category	Parameter	Symbol	Value
PMSG	Machine resistance	R_S	1.058 mΩ
	Machine inductance	L_S	99 μH
	Permanent magnet flux linkage	ϕ_m	0.03644 V*s/rad
	Number of poles	p	6
	Nominal power	P_N	45 kW
Cable	Local capacitor	C_l	1.6 mF
	Cable resistor	R_C	3 mΩ (0.6 mΩ/m)
	Cable inductor	L_C	1 μH (0.2 μH /m)
Main bus	Bus Capacitor	C_b	0.5 mF
Droop characteristic	Nominal voltage	V_o	270 V
	Droop slope	k_D	8.5
Stator current loop	Proportional gain	K_{idp}, K_{iqp}	0.8785
	Integral gain	K_{idi}, K_{iqi}	3908
Flux weakening	Proportional gain	K_{vcp}	0
	Integral gain	K_{vci}	5000
DC current control	Proportional gain	K_{iop}	0.4
	Integral gain	K_{ioi}	600

REFERENCES

[1] J. A. Rosero, J. A. Ortega, E. Aldabas, and L. Romeral, "Moving towards a more electric aircraft," *IEEE Aerosp. Electron. Syst. Mag*., vol. 22, no. 3, pp. 3–9, Mar. 2007.

[2] P. Wheeler and S. Bozhko, "The more electric aircraft: technology and challenge," *IEEE Electrif. Mag*., vol. 2, no. 4, pp. 6–12, Dec. 2014.

[3] D. Salomonsson and A. Sannino, "Low-voltage dc distribution system for commercial power systems with sensitive electronic loads," *IEEE Trans. Power Del*., vol. 22, no. 3, pp. 1620–1627, Jul. 2007.

[4] A. Kwasinski, "Quantitative evaluation of dc microgrids availability: Effects of system architecture and converter topology design choices," *IEEE Trans. Power Electron*., vol. 26, no. 3, pp. 835–851, Mar. 2011.

[5] A. Emadi, A. Khaligh, C. Rivetta, and G. Williamson, "Constant power loads and negative impedance instability in automotive systems: Definition, modeling, stability, and control of power electronic converters and motor drives," *IEEE Trans. Veh. Technol*., vol. 55, no. 4, pp. 1112–1125, Jul. 2006.

[6] A. Rahimi and A. Emadi, "An analytical investigation of dc/dc power electronic converters with constant power loads in vehicular power systems," *IEEE Trans. Veh. Technol*., vol. 58, no. 6, pp.2689–2702, Jul. 2009.

[7] A. M. Rahimi, G. A. Williamson, and A. Emadi, "Loop-cancellation technique: A novel nonlinear feedback to overcome the destabilizing effect of constant-power loads," *IEEE Trans. Veh. Technol*., vol. 59, no. 2, pp. 650–661, Feb. 2010.

[8] P. Magne, B. Nahid-Mobarakeh, and S. Pierfederici, "General active global stabilization of multiloads dc-power networks," *IEEE Trans. Power Electron*., vol. 27, no. 4, pp. 1788–1798, Apr. 2012.

[9] K-N. Areerak, T. Wu, S. V. Bozhko, G. M. Asher, and D. W. P. Thomas, "Aircraft power system stability study including effect of voltage control and actuators dynamic," *IEEE Trans. Aerosp. Electron. Syst*., vol. 47, no. 4, pp. 2574–2589, Oct. 2011.

[10] L. Han, J. Wang, and D. Howe, "Small-signal stability studies of a 270V dc more-electric aircraft power system," in *Proc. Power Electronics Machines and Drives 2006. The 3rd IET International Conference*, Ireland, Apr. 2006, pp. 197–201.

[11] J. M. Guerrero, M. Chandorkar, T.-L. Lee, and P. C. Loh, "Advanced control architectures for intelligent microgrids–Part I: Decentralized and hierarchical control," *IEEE Trans. Ind. Electron*., vol. 60, no. 4, pp. 1254–1262, Apr. 2013.

[12] B.-F. Wu, H.-I. Chin, J.-W. Perng, and T.-T. Lee, "Robust control design for perturbed systems by frequency domain approach," *IEEE Trans. Veh. Technol*., vol. 56, no. 5, pp. 2893–2901, Sep. 2007.

[13] B. Demirel and L. Güvenc, "Parameter space design of repetitive controllers for satisfying a robust performance requirement," *IEEE Trans. Automat. Contr*., vol. 55, no. 8, pp. 1893–1899, Aug. 2010.

[14] S. Sonmez and S. Ayasun, "Stability region in the parameter space of PI controller for a single-area load frequency control system with time delay," *IEEE Trans. Power Syst*., vol. 31, no. 1, pp. 829–830, Jan. 2016.

[15] F. Gao, X. Zheng, S. Bozhko, C. Hill, and G. Asher, "Modal analysis of a PMSG-based dc electrical power system in the more electric aircraft using eigenvalues sensitivity," *IEEE Trans. Transp. Electrif*., vol. 1, no. 1, pp. 65–76, Jun. 2015.

[16] Department of Defense of United States of America, "Department of defense interface standard–aircraft electric power characteristics," *Military Std. MIL-STD-704F*, USA, Mar. 2004.

[17] F. Gao, S. Bozhko, A. Costabeber, C. Patel, P. Wheeler, C. Hill, and G. Asher, "Comparative stability analysis of droop control approaches in voltage source converters-based DC microgrids," *IEEE Trans. Power Electron*., vol. 99, no. 99, pp. 1-1, 2016.